Statistical analysis for EUV dynamic spectra and their impact on the ionosphere during solar flares

Shohei Nishimoto[1], Kyoko Watanabe[1*] , Hidekatsu Jin[2], Toshiki Kawai[3], Shinsuke Imada[4], Tomoko Kawate[5], Yuichi Otsuka[3], Atsuki Shinbori[3], Takuya Tsugawa[2] and Michi Nishioka[2]

Abstract

The X-rays and extreme ultraviolet (EUV) emitted during solar flares can rapidly change the physical composition of Earth's ionosphere, causing space weather phenomena. It is important to develop an accurate understanding of solar flare emission spectra to understand how it affects the ionosphere. We reproduced the entire solar flare emission spectrum using an empirical model and physics-based model, and input it into the Earth's atmospheric model, GAIA to calculate the total electron content (TEC) enhancement due to solar flare emission. We compared the statistics of nine solar flare events and calculated the TEC enhancements with the corresponding observed data. The model used in this study was able to estimate the TEC enhancement due to solar flare emission with a correlation coefficient greater than 0.9. The results of this study indicate that the TEC enhancement due to solar flare emission is determined by soft X-ray and EUV emission with wavelengths shorter than 35 nm. The TEC enhancement is found to be largely due to the change in the soft X-ray emission and EUV line emissions with wavelengths, such as Fe XVII 10.08 nm, Fe XIX 10.85 nm and He II 30.38 nm.
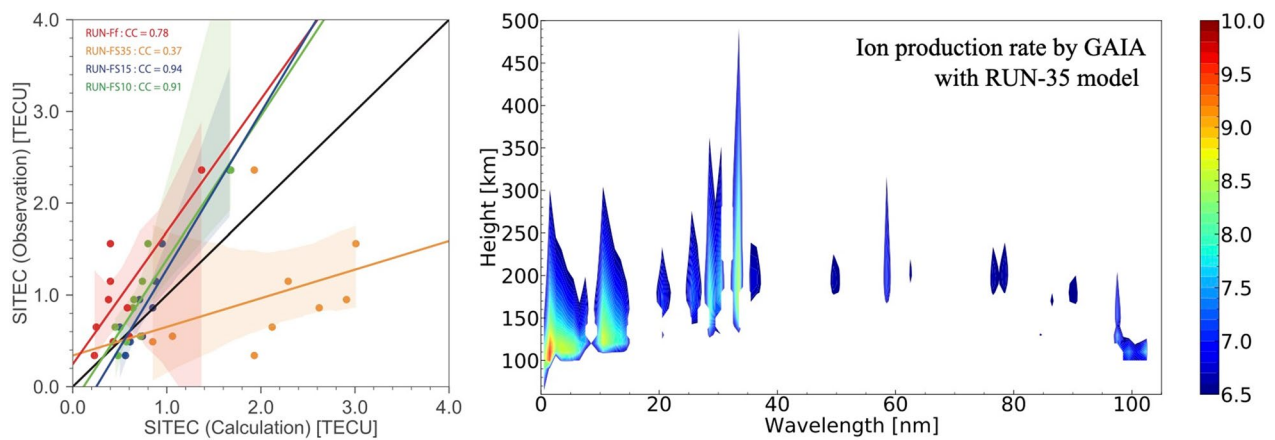
Keywords Solar flare, X-ray emission, EUV emission, Ionosphere, Space weather

*Correspondence:
Kyoko Watanabe
kwatana@nda.ac.jp
Full list of author information is available at the end of the article

Nishimoto *et al. Earth, Planets and Space*   (2023) 75:30

Page 2 of 15

Graphical Abstract

Introduction

Solar flares have a significant impact on the solar-terrestrial environment. An accurate understanding of the relationship between solar flare emissions and Earth's ionosphere is important for the safe construction and use of space infrastructure. When a solar flare occurs, electromagnetic emission in X-ray and EUV wavebands. In particular, it is well-known that X-rays (0.1–10 nm) and extreme ultraviolet (EUV) (10–121.6 nm) emitted during solar flares, enhanced to several 10 to a 1000 and sometimes to 10,000 during flare events, affect the Earth's ionosphere. The phenomena caused by the sudden ionization of the Earth's upper atmosphere by X-rays and EUV emitted from solar flares are widely known as sudden ionospheric disturbances (SIDs) (Davies 1990; Donnely 1969; Mitra 1974). SIDs are sudden disturbances of the ionosphere and are a superset of events, which consists of Dellinger effect (Dellinger 1937), short-wave fadeout (SWF) (e.g., Chakraborty et al. 2018, 2019, 2022; Fiori et al. 2018, 2022), sudden frequency and phase deviation (SFD/SPD) (Chakraborty et al. 2018; Watanabe and Nishitani 2013), solar flare effects (SFEs) (e.g., Curto et al. 2018), and sudden increase in total electron content (SITEC) (e.g., Tsugawa et al. 2006; Zhang et al. 2011). In 1957, the International Geophysical Year, much was offered from around the world on SIDs, and research in this field began to advance dramatically (Curto 2020).

The solar emission spectrum and the physical properties of the Earth's ionosphere are closely related, and the wavelength of solar emission determines the altitude at which the neutral atmosphere in the ionosphere is ionized. The soft X-rays and EUV emissions with wavelengths shorter than 25 nm, mainly emitted from the optically thin solar corona, increase rapidly during solar flares and affect the Earth's lower ionosphere (~150 km) (Qian et al. 2011). EUV emissions at wavelengths of 26–34 nm emitted from the optically thick transition layer and chromosphere primarily ionize the atomic oxygen in the F region, at altitudes above ~200 km (e.g., Qian et al. 2011; Richards et al. 1994; Woods et al. 2011). The characteristic of solar flare emissions referred to as the center-to-limb variation (CLV) describes the phenomenon in which the optically thick EUV emission weakens toward the edge of the solar disk, while the optically thin emission is unaffected (e.g., Woods et al. 2006; Worden et al. 2001). Therefore, flare location on the solar disk is an important parameter that determines the TEC variability, as solar flares occurring in the center of the solar disk have a relatively greater impact on the Earth's ionosphere than those occurring at the limb (Qian et al. 2010, 2019; Zhang et al. 2011). Qian et al. (2011) investigated the relationship between solar flare duration and the ionospheric response and found that solar flares with longer durations (i.e., solar flares with higher total energy) have a greater impact on the ionosphere.

To understand the relationship between solar flare emissions and ionospheric response, the entire solar emission spectrum must be considered, not just the solar flux in one or limited number of wavebands. This is not only because the ionospheric variability due to solar flare emissions is intrinsically dependent on solar emission of the wavelength range from X-rays to EUV, but also because the solar flare emission spectrum varies greatly from event to event (Tsurutani et al. 2009; Zhang et al. 2011). Soft X-ray emissions have been observed continuously since 1975 by the X-ray Sensor (XRS) onboard

Nishimoto *et al. Earth, Planets and Space*   (2023) 75:30

Page 3 of 15

the Geostationary Operational Environmental Satellite (GOES). GOES/XRS observes two wavelength bands, 0.05–0.4 nm and 0.1–0.8 nm, with a time resolution of ~ 2 s (Bornmann et al. 1996). EUV emissions have been observed since the 1990s, using a variety of instruments. The Solar Dynamics Observatory (SDO), launched in February 2010, is equipped with an extreme ultraviolet variability experiment (EVE) (Woods et al. 2012). The multiple EUV grating spectrograph (MEGS), a subsystem of SDO/EVE, measures the full-disk solar irradiance in the range 5–106 nm, with a spectral resolution of 0.1 nm and a time cadence of 10 s, since May 2010. MEGS-A, which observed 5–37 nm, was shut down in May 2014 due to a malfunction. MEGS-B, which observes 35–105 nm, is still in operation, but it only observes for ~ 3 h a day and does not always provide high-resolution EUV emission spectra during solar flares.

Various models have been developed to estimate the unobserved X-ray and EUV emissions from the Sun. The flare irradiance spectral model (FISM) is currently the most widely used model (Chamberlin et al. 2007, 2008, 2020). FISM2, newly released in 2020, is an empirical model which uses the latest observations, and has improved both estimation accuracy and resolution compared to the previous model. FISM2 is used as the empirical model for this study, which is describe in detail in Sect. "FISM2". Kawai et al. (2020) introduced a new method to reproduce the emission spectrum of EUV flares, which is called the solar flare emission model (Kusano et al. 2021). In this paper, the solar flare emission model is referred to as the SFEM. The SFEM is based on the physical process of the time variation of the plasma distribution in the flare loop, which is the primary source of the flare emission. Nishimoto et al. (2021) statistically validated that the SFEM can reproduce the flare emission energy and time evolution of the EUV line emission. One advantage of a physics-based model is that it allows us to consider whether the physical processes assumed by the model are correct. The detail of the SFEM is explained in section "data".

The purpose of this study is to investigate which wavelengths of solar emissions control the Earth's ionospheric state by reproducing the TEC enhancements caused by solar flare emissions and comparing them with observations. We reproduced the entire solar flare emission spectrum using FISM2 and the SFEM. The data were then input into an Earth's atmospheric model to calculate the TEC enhancement. We used the Earth's atmospheric model, which is called the Ground-to-Topside Model of Atmosphere and Ionosphere for Aeronomy (GAIA; Jin et al. 2011). We compared nine solar flare events and calculated the TEC enhancements with the corresponding observed data. This paper is organized as follows:

section "Data" introduces the solar emission spectrum models and the Earth's atmospheric model, GAIA used in this study, as well as the TEC observation data. Section "Data analysis and results" shows an example of the model simulation to reproduce the TEC enhancement, and identifies the wavelength of the solar flare emission that determines the TEC enhancement by showing the statistical results and comparing the calculation results with the observation results. Section "Discussion and summary" discusses and summarizes the results of this comparison.

Data
We analyzed nine solar flare events from the Hinode Flare Catalogue (Watanabe et al. 2012) that met the following criteria: (1) the observation period is from 2010 to 2021; (2) the scale of the flare is larger than that of the X class; and (3) the distance between flare ribbons can be observed by the SDO/Atmospheric Imaging Assembly (AIA) (Lemen et al. 2012). For these solar flare events, we used soft X-ray flux observations by GOES/XRS, EUV emission spectrum observations by SDO/EVE, emissions synthesized by FISM2, and the SFEM. Note that events whose TEC enhancement is equal to or greater than the variability before the flare start were not used in the analysis of this study.

Solar flare emission spectral models
FISM2
The most widely used solar emission spectrum model is the Flare Irradiance Spectral Model (FISM) (Chamberlin et al. 2007, 2008). The first version of FISM was released in 2005. FISM is an empirical model of the solar emission spectrum irradiance, which provides a "daily component" to estimate the solar emission variation due to the solar cycle and solar rotation, and a "flare component" that adds the variation due to solar flares. FISM uses the GOES soft X-ray flux and the time derivative of the GOES soft X-ray flux are used as a proxy of the gradual phase and the impulsive phase of the flare, respectively. FISM2 (version 2 of the FISM) was released in 2020, estimating the solar flare emission spectra in the wavelength range of 0–190 nm with a 0.1 nm spectral resolution and 60 s cadence (Chamberlin et al. 2020). Proxy data used for the FISM2 daily component include not only the 10.7 cm radio flux, but also the MgII core/wing ratio (Snow et al. 2005) and the H I Lyman-α emission line. FISM2 could reproduce EUV emission spectra with high accuracy due to its incorporation of thousands of events of flare emission data based on high-precision and high-resolution observation data, such as SDO/EVE. However, Chamberlin et al. (2020) reported that FISM2 is unable to reproduce the time evolution of EUV line emission

Nishimoto *et al. Earth, Planets and Space*   (2023) 75:30

Page 4 of 15

with a high formation temperature, which dominates the gradual phase of the flare. This was because FISM considers the time evolution of all EUV emission lines to be the same as the time evolution of the GOES soft X-ray flux or derivative of the GOES soft X-ray flux, which is a proxy; moreover, the cooling of the flare loops (time difference of EUV emission lines) was not well-represented. FISM2 plans to solve the problem using an empirical correction found using the enthalpy-based thermal evolution of loops (EBTEL) model, a zero-dimensional hydrodynamic model that can calculate the temperature and density in flare loops without calculating the spatial evolution of loops (Cargill et al. 2012; Chamberlin et al. 2020; Klimchuk et al. 2008; Thiemann et al. 2017). In this study, we used FISM2 daily as the solar background emission and FISM2 flare, which includes the background emission, as the flare emission.

Solar flare emission model (SFEM)

We developed a simplified model based on the physical processes of flare loops (Kawai et al. 2020). In this model, the GOES soft X-ray flux observations during flare were converted into EUV emission spectra using the one-dimensional hydrodynamic model called the CANS 1D package   (http://www.astro.phys.s.chiba-u.ac.jp/netlab/astro/) and the CHIANTI atomic database (version 9.0) (Dere et al. 1997, 2019). As a result of the statistical comparison between the SFEM and SDO/EVE observations, the SFEM reproduces the flare time-integrated emission of EUV flares corresponding to the flare emission energy, and the flare rise time corresponding to the flare duration for Fe lines with correlation coefficients of 0.83–0.96 and 0.86–0.95, respectively (Nishimoto et al. 2021). The main parameters of the SFEM used in this study are the half-loop length and the input energy. We determined the half-loop length from the observed ribbon distance with the SDO/AIA 160 nm, and the input energy was determined by scaling the magnitude of the synthesized soft X-ray light curves to the GOES/XRS observations. The default parameter values of CANS 1D were used for the others (see Section "Discussion and summary" in Nishimoto et al. 2021).

Ionospheric TEC observation and GAIA model

In this study, TEC was used to evaluate the response of the Earth's ionosphere to solar flares. TEC has been recommended as an important ionospheric parameter that can be used to assess predictive capability with respect to space weather (Goncharenko et al. 2021; Scherliess et al. 2019). The TEC is a physical quantity that represents the total number of electrons per unit area integrated along the line of sight between the global navigation satellite system (GNSS) satellite and the receiver. It was calculated using the distance between satellite and receiver, as the time delay is proportional to the integral of the plasma density along the propagation path from the satellite to the receiver (Otsuka et al. 2002; Shinbori et al. 2020; Tsugawa et al. 2018). The relative observation accuracy of this TEC is 0.02 TEC unit (TECU) (Hofmann-Wellenhof et al. 1992). One TECU equals 10^{12} electrons cm^{-2}. We used the TEC observation data provided by the National Institute of Information and Communications Technology (NICT) and Nagoya University.

We used the Earth's atmospheric model, GAIA, to study the TEC variations caused by different flare emission spectra. The GAIA is constructed by combining the whole atmospheric general circulation model (GCM) (Fujiwara and Miyoshi 2006, 2009, 2010; Miyoshi and Fujikawa 2003, 2006, 2008), the ionospheric model (Shinagawa et al. 2007; Shinagawa and Oyama 2006), and an electrodynamics model (Jin et al. 2008). The GCM treats physical processes suitable for the troposphere, stratosphere, mesosphere, and thermosphere as neutral atmospheric regions. The horizontal grid spacing was 2.8°, the vertical resolution was 0.2 scale heights above the tropopause, and the temporal resolution was 20 s. The ionospheric model solves the mass, momentum, and energy equations for the major ions and electrons. The horizontal grid spacing is 2.5° in the longitude direction, 1° in the latitude direction, 10 km in the vertical direction up to 600 km, and the time resolution is 1–4 s. The electromagnetic model treats the global ionospheric current induced by the neutral wind dynamo and polarization electric field. The model assumes that the geomagnetic field lines are equipotential and that the current dissipates at the low-altitude boundary (70 km) and is conserved along the magnetic field lines between the north and south high-altitude boundaries (720 km) along the same magnetic field lines. The horizontal grid spacing at an altitude of 70 km is 2.8° in the longitude direction and 0.2–0.6° in the latitude direction. The coupling between the three model components was achieved by introducing a main module called the "coupler" and arranging each model component in the form of an FORTRAN subroutine or module and calling it in the coupler program. The coupler handles the general procedures for running the integrated model, such as setting common parameters and conditions, controlling time increment, and exchanging physical variables between model components. Since the time and grid resolution of each model is different, the coupler module is used to perform coordinate transformations in variable exchanging. The latest version of GAIA allows solar emission spectra, rather than single wavelength solar emission, to be input to simulate the response of the Earth's atmosphere, including the

Nishimoto *et al. Earth, Planets and Space* (2023) 75:30

Page 5 of 15

ionosphere. The ionization cross sections of the atoms and molecules that make up the ionosphere, corresponding to each wavelength of solar emission, are given by Solomon and Qian (2005).

Data analysis and results

We input the EUV flare emission spectra from FISM2 and the model proposed by Kawai et al. (2020) into GAIA to reproduce the TEC enhancements due to flare events, and compared the calculated results with the observations. First, among the nine flare events analyzed in this study, we present the results of the case study analysis
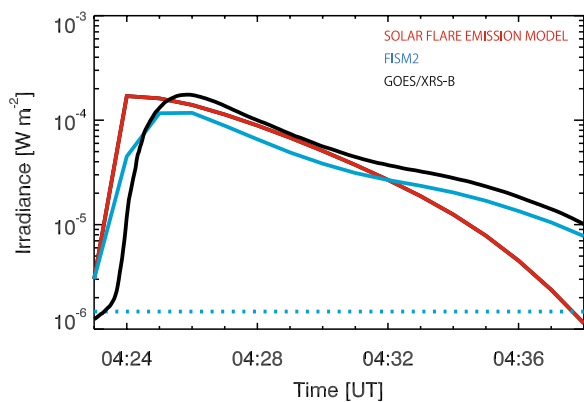
that illustrate the response of the ionosphere to different solar flare emission spectra, followed by the results of the statistical analysis.

Figure 1 displays an example of the observed and reproduced light curves of GOES/XRS-B during the X1.1-class flare on November 8, 2013. The solid red, blue, and black lines indicate the light curves obtained from the SFEM, the flare component of FISM2 (FISM2 flare), and the GOES/XRS observation, respectively. The dotted blue line indicates the daily component of FISM2 (FISM2 daily). Figure 1 shows that the magnitude of the soft X-ray flux is accurately represented in the SFEM, and the time evolution of FISM2 is also accurately reproduced, because GOES/XRS is used as a proxy. The following correction was made when inputting the emission spectrum obtained by the SFEM into the GAIA. When the emission intensity was smaller than that of FISM2 daily, it was replaced by FISM2 daily. This is because the flare emission spectrum of the SFEM tends to decay rapidly around the flare end time, as it roughly and virtually reproduces the multi-flare loop emission from the calculated single-flare loop (see Sect. 4.4 of Nishimoto et al. 2021).

Figure 2 displays an example of the observed and reproduced flare time-integrated spectra and the ratio of the observed data to the calculated data for the X1.1-class flare on November 8, 2013. The solid blue, red and black lines indicate the flare time-integrated spectrum obtained from the FISM2 flare, SFEM, and SDO/EVE MEGS-A observations, respectively. As shown in Fig. 2a, the SFEM and FISM2 both reproduce the observed trend. However, the value of the SFEM becomes significantly smaller when the wavelength is longer than ∼70 nm, because the SFEM does not consider the reproduction

Fig. 1 Example of the observed and modeled soft X-ray fluxes of GOES/XRS-B. The soft X-ray fluxes of GOES/XRS-B during the X1.1-class flare on November 8, 2013. The solid red, blue, and black lines indicate the light curves obtained from the SFEM, the flare component of FISM2 (FISM2 flare), and the GOES/XRS observation, respectively. The dotted blue line indicates the daily component of FISM2 (FISM2 daily)

Fig. 2 Example of the flare time-integrated spectra and ration of the observed and calculated data. **a** Flare time-integrated spectra and **b** ratio of the observed data to the calculated data for the X1.1-class flare on November 8, 2013. The solid red, blue, and black lines indicate the flare time-integrated spectrum obtained from the SFEM, the FISM2 flare, and the SDO/EVE MEGS-A observation, respectively. The solid black line in **b** shows the line with a ratio of 1

Nishimoto *et al. Earth, Planets and Space* (2023) 75:30

Page 6 of 15

of the optically thick emission or the continuum component emitted from the solar atmosphere at altitudes lower than the transition region. The emission intensity of the optically thick SFEM is larger than that of FISM2 in the soft X-ray region, where the wavelength is shorter than 10 nm. Figure 2b shows that FISM2 reproduces the observed flare time-integrated irradiance for the wavelength range of 5–37 nm accurately. However, at wavelengths of 10–11 nm, 28–29 nm, and 32–34 nm, the SFEM is more than twice as large as the observed values.

Previous studies have suggested that X-ray and EUV emissions at wavelengths shorter than 45 nm are important indicators of the response of the Earth's ionosphere (Woods et al. 2011; Zhang et al. 2011). Therefore, in this study, we focused on the 5–35 nm region observed by SDO/EVE MEGS-A, which has a strong intensity emission during flare and input five types of solar flare emission spectra into the GAIA using FISM2 and the SFEM to investigate in detail the wavelengths of solar emission that determine TEC enhancements. The five types of flare emission spectra input to the GAIA are as follows: the FISM2 daily (RUN-Fd), the FISM2 flare (RUN-Ff), the FISM2 flare replaced by the SFEM at wavelengths shorter than 35 nm (RUN-FS35), the FISM2 flare replaced by the SFEM at wavelengths shorter than 15 nm (RUN-FS15), and the FISM2 flare replaced by the SFEM at wavelengths shorter than 10 nm (RUN-FS10).

Figures 3 and 4 show the TEC distribution of each RUN and its ratio to RUN-Fd at 130°E, where the local time is around noon when the flare occurs. These figures show that RUN-Fd shows no TEC enhancement due to flare emission, while RUN-Ff, RUN-FS15, RUN-FS10, and RUN-FS35 reproduce TEC enhancement due to flare emission. The spatial–temporal variation of TEC in RUN-Fd, which does not contain a flare emission, is because TEC varies with the solar zenith angle. Thus, we can see that the TEC simulation by GAIA model is working well.

Figures 5 and 6 show the difference in ion production rates between the pre-flare and the flare peak calculated with RUN-Ff and RUN-FS35 for the X1.1 class flare on November 8, 2013, respectively. These figures show that the neutral atmospheric compositions are ionized mainly by flare emission with wavelengths shorter than 35 nm. It is clear that the ion production rate of RUN-FS35 was greater than that of RUN-Ff. The major difference between RUN-Ff and RUN-FS35 is the difference in ion production rates of O^+, N^+, and N_2^+ at wavelengths shorter than 10 nm and around 10–15 nm that ionize the D and E regions, and O^+ and N^+ corresponding to solar emission at 25–35 nm that ionize the F region. The difference in ion production rates between RUN-Ff and RUN-FS35 corresponds to the wavelength region, where the intensity of solar flare emission by the SFEM is generally larger than the observed value (see Fig. 2).

Statistical result for TEC enhancement due to flare emission

We compared the difference of TEC (DTEC), which indicates TEC enhancement due to flare emission obtained from the GAIA calculations and the observations for nine flare events. The flare parameters and TEC parameters
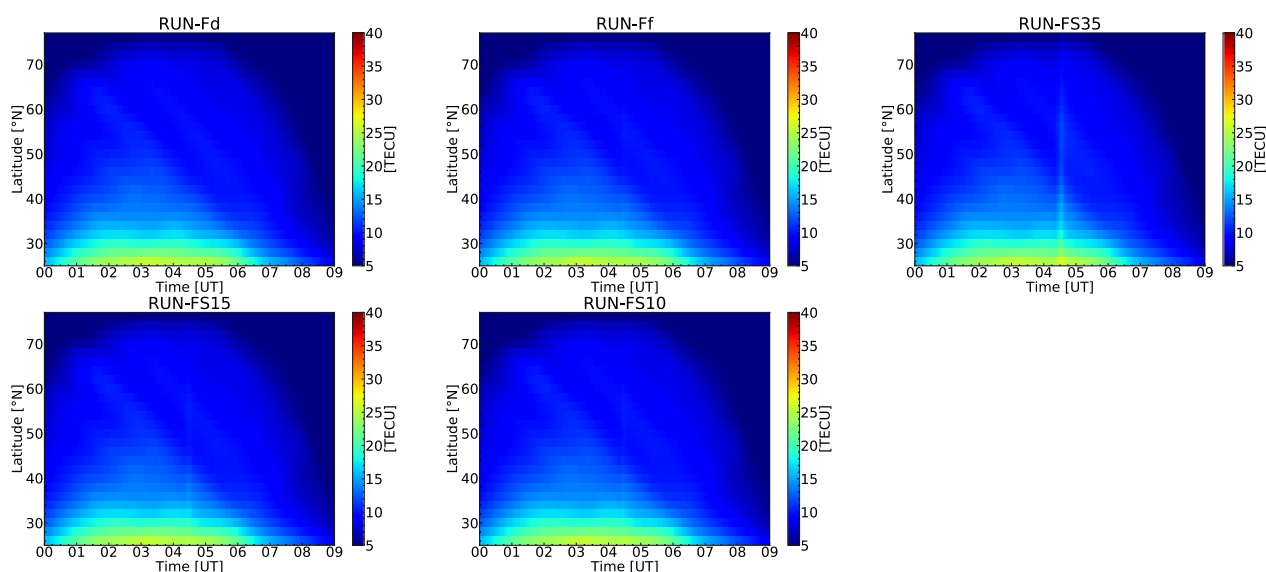
Fig. 3 TEC simulated by GAIA model. The TEC distributions for RUN-Fd, RUN-Ff, RUN-FS35, RUN-FS15, and RUN-FS10 at 130°E, where, locally, at the time of the flare are around noon for the X1.1-class flare on November 8, 2013
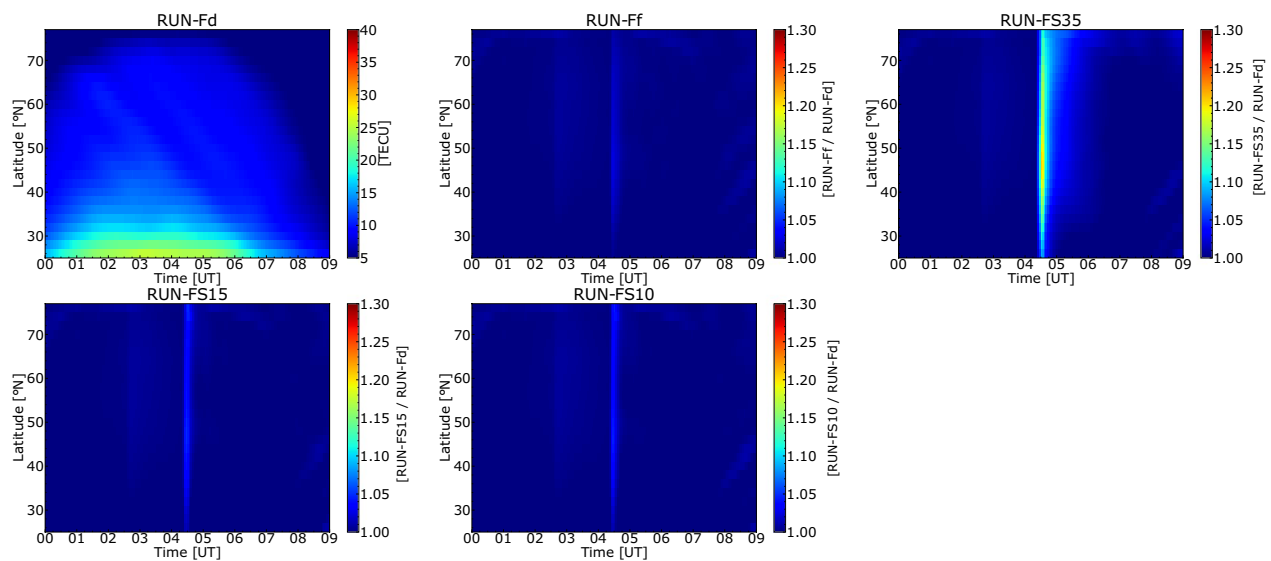
Fig. 4 Ratio of TEC distribution calculated by GAIA. The ratio of TEC distribution calculated by RUN-Fd for RUN-Ff, RUN-FS35, RUN-FS15, and RUN-FS10 at 130°E around noon local time at the time of the flare shown in Fig. 3 for the X1.1-class flare on November 8, 2013

of these flare events are listed in Table 1. The DTEC observed and calculated values were obtained when the local time was around noon when each flare event occurred. The DTEC of observational data was derived by subtracting the running average for 30 min from the absolute TEC value. As the TEC value obtained from the GNSS carrier phase is relative, a correction is required to obtain the absolute value. The absolute TEC value is obtained by the method proposed by Shinbori et al. (2020). First, the TEC value calculated using the carrier phase was adjusted to the level of the TEC value calculated using the two pseudo-ranges. However, as this value contains the instrumental bias, it is necessary to estimate the instrumental bias to obtain the absolute value of the TEC. This bias was estimated by the hourly TEC average and the interfrequency bias using the weighted least-squares fitting of the relative TEC values obtained from each GNSS station and excluded from the relative TEC values (Otsuka et al. 2002). For the DTEC of calculation data, the TEC value of RUN-Fd, which does not contain a flare component, was subtracted from the TEC calculation value of each RUN. In this study, SITEC value is defined to quantitatively evaluate the TEC enhancement due to flare as the difference between the minimum value of DTEC around the flare start time and the maximum value of DTEC during the flare.

Figure 7 displays the time variation of the DTEC for the nine flare events. The solid black, dashed red, orange, blue, and green lines indicate the DTEC obtained from the observations, RUN-Ff, RUN-FS35, RUN-FS15, and RUN-FS10, respectively. The DTEC

observed and calculated values were obtained at the point, where the local time was around noon when each flare event occurred. To derive the DTEC, we subtracted the 30-min running average from the absolute TEC observational data. For the calculation data, the TEC value of RUN-Fd, which does not contain flare component, was subtracted from the TEC calculation value of each RUN. In this study, SITEC is defined as the difference between the minimum value of DTEC around the flare start time and the maximum value of DTEC during the flare. As shown in Fig. 7, the DTEC increases with the start of the flare, and the observed SITEC variation is 0.34–2.36 TECU. This variable value of SITEC is reasonable in comparison with previous studies (e.g., Qian et al. 2011; Yasyukenvich et al. 2018; Zhang et al. 2011).

Figure 8 shows the relationship between the observed and calculated SITECs for the nine flare events. The results of RUN-Ff, RUN-FS35, RUN-FS15, and RUN-FS10 are plotted in red, orange, blue, and green, respectively. The dashed line indicates the regression of each plot, and the black solid line indicates a straight line with a slope of 1. The correlation coefficients (CC) for RUN-Ff, RUN-FS35, RUN-FS15, and RUN-FS10 were 0.78, 0.37, 0.94, and 0.91, respectively. The mean absolute errors (MAE) between the line with slope 1 and the regression line were 0.49, 1.19, 0.28, and 0.33 for RUN-Ff, RUN-FS35, RUN-FS15, and RUN-FS10, respectively. Note that we show a more robust maximal information coefficient (MIC) due to the small number of analysis events; MIC is a measure of the dependence between
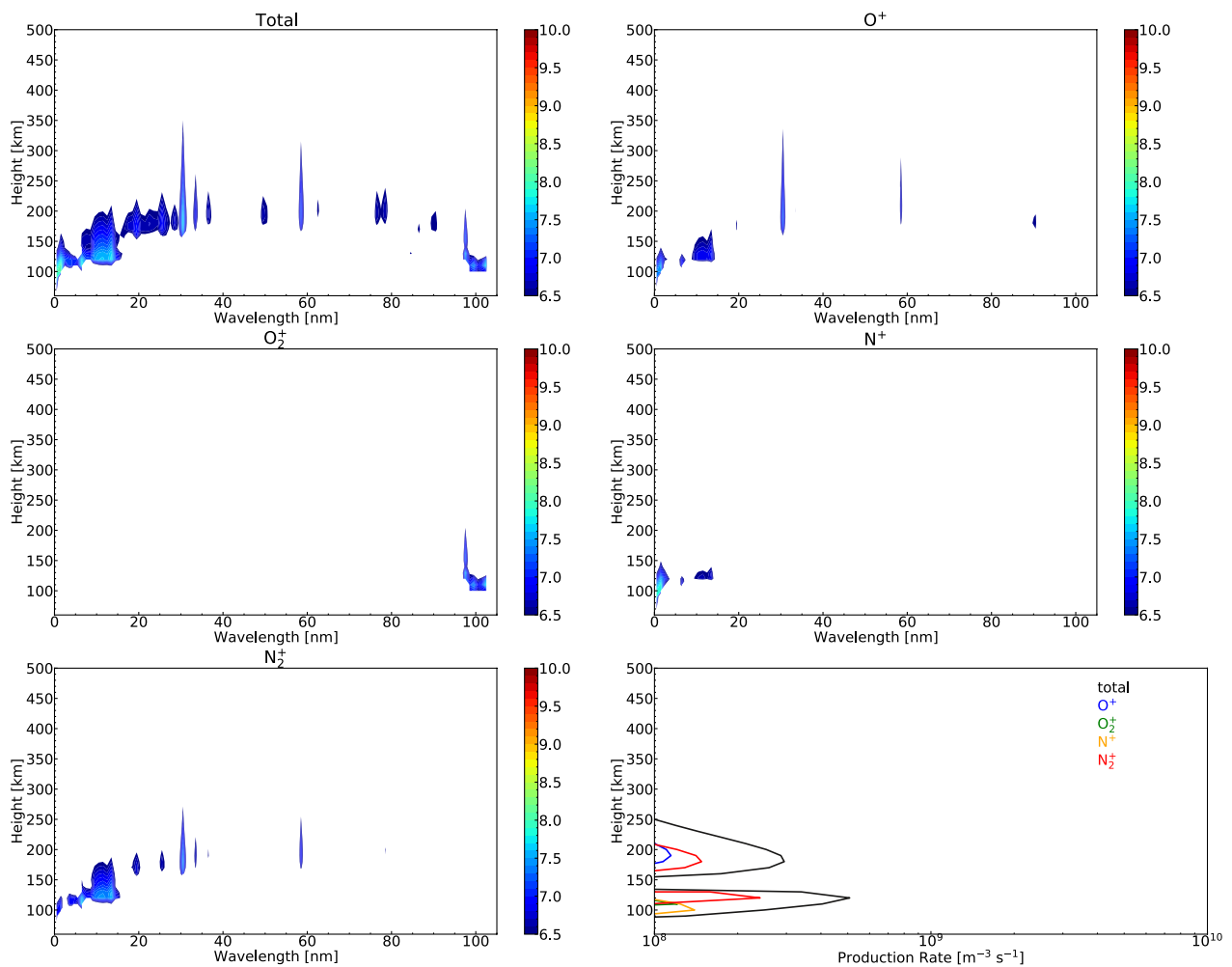
Fig. 5 Differences in ion production rate between the pre-flare and flare peak by GAIA with RUN-Ff. Differences in ion production rate between the pre-flare and flare peak at 130°E and 34°N calculated by GAIA with RUN-Ff for the X1.1 class flare that occurred on November 8, 2013. Differences in the ionization rates for **a** total ion, **b** O^+, **c** O_2^+, **d** N^+, **e** N_2^+ as a function of the wavelength of solar emission (unit: Log10 (W m^{-2} nm^{-1}). **f** Differences in the altitude distribution of the ionization rates of each ion. The solid and dotted lines indicate the ionization rates of each ion at the flare peak (4:24 UT) and the pre-flare (4:00 UT), respectively

two variables and calculates the grid delimitation that maximizes the value of the mutual information content and its maximum value (Reshef et al. 2011). The MIC for RUN-Ff, RUN-FS35, RUN-FS15, and RUN-FS10 were 0.32, 0.59, 0.59, and 0.59, respectively. The results showed that RUN-FS15 and RUN-FS10 effectively reproduced the observed values of the SITEC.

Figure 9 shows the relationship between the solar emission wavelength and the difference in ion production rate investigated using RUN-FS15, which best reproduces the SITEC observations in Fig. 8. Figure 9 indicates that the solar emission that contributes the most significantly to the TEC enhancement during flares is soft X-ray emission with wavelengths shorter than 10 nm. For EUV emission, the wavelengths of 10–15 nm and 30–35 nm

contribute to the improvement of TEC. For most flare events, the ion production rate peaks at 1–2 nm in soft X-ray emission, and at 10–11 nm and 30–31 nm in EUV emission. The ratios of integrated ion production rate by EUV emission with wavelengths of 10–15 nm and 30–35 nm to integrated ion production rate by soft X-ray emission with wavelengths shorter than 10 nm, obtained from Fig. 9, were 12.4–23.8% (average 18.8%) and 0.5–23.1% (average 6.5%), respectively.

Discussion and summary

We used a solar flare emission spectral model with a wavelength resolution of 0.1 nm and the Earth's atmospheric model to reproduce the response of Earth's ionosphere to solar flare emission and to identify the
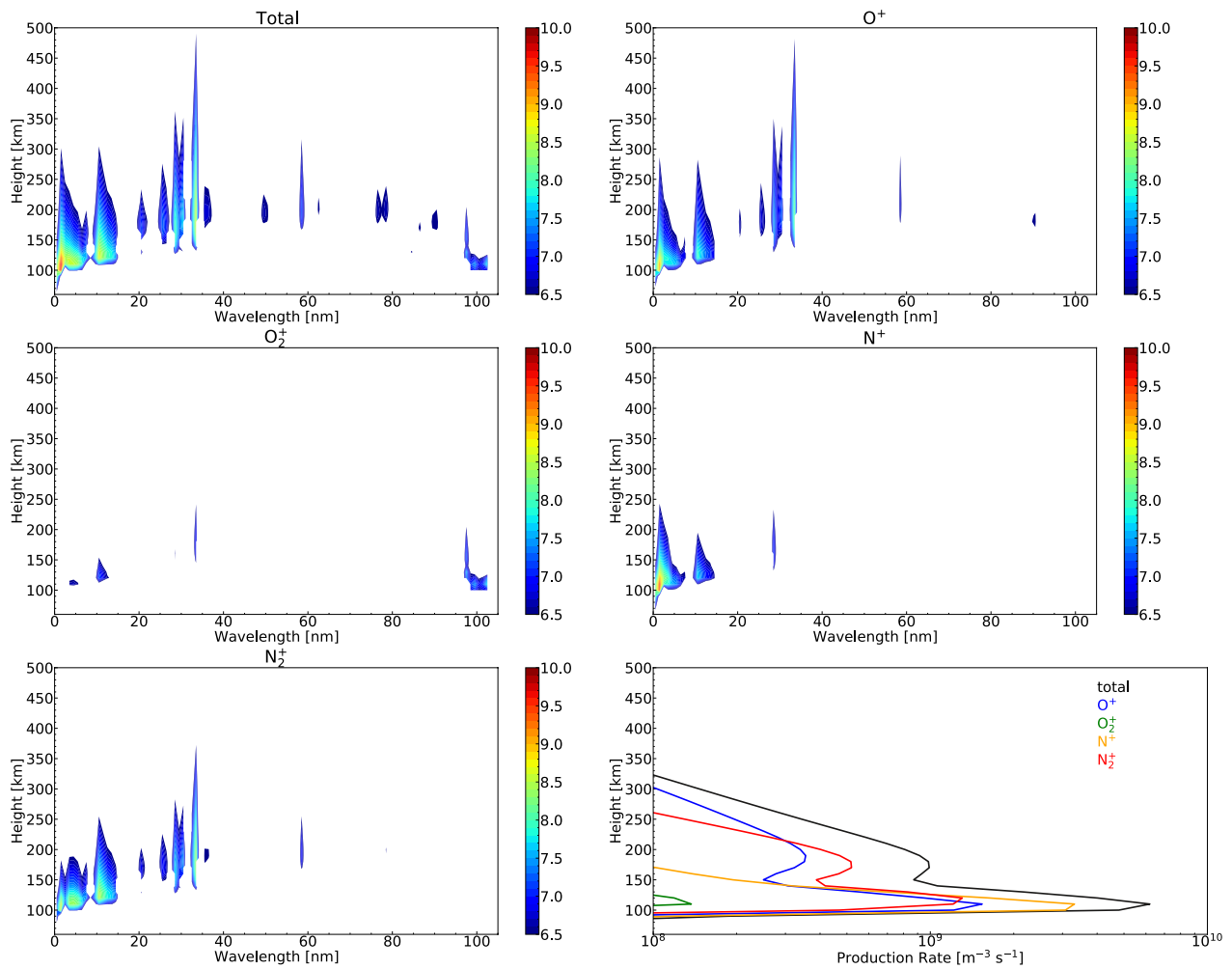
Fig. 6 Differences in ion production rate between the pre-flare and flare peak by GAIA with RUN-35. Differences in ion production rate between the pre-flare and flare peak at 130°E and 34°N calculated by GAIA with RUN-FS35 for the X1.1 class flare that occurred on November 8, 2013. Differences in the ionization rates for **a** total ion, **b** O^+, **c** O_2^+, **d** N^+, **e** N_2^+ as a function of the wavelength of solar emission (unit: Log10 (W m^{-2} nm^{-1}). **f** Differences in the altitude distribution of the ionization rates of each ion. The solid and dotted lines indicate the ionization rates of each ion at the flare peak (4:24 UT) and the pre-flare (4:00 UT), respectively

Table 1 Flare parameters and TEC parameters for the nine flare events analyzed in this study

Date	GOES class	Flare start time [UT]	Flare peak time [UT]	Flare end time [UT]	SITEC [TECU]	TEC observation point [deg]
6 September 2017	X9.3	11:55:12	12:02:14	12:22:00	2.36	44°N0°E
5 November 2013	X3.3	22:10:39	22:11:51	22:20:39	1.56	40°S175°E
6 September 2017	X2.2	9:01:09	9:10:25	9:22:32	0.55	44°N10°E
11 March 2015	X2.1	16:15:26	16:21:42	16:49:21	1.15	44°N72°W
7 November 2014	X1.6	17:09:47	17:26:02	17:39:59	0.86	42°N75°W
7 September 2017	X1.3	14:35:30	14:39:58	14:53:00	0.49	44°N72°W
8 November 2013	X1.1	4:23:30	4:24:44	4:39:59	0.65	34°N130°E
10 November 2013	X1.1	5:10:33	5:12:38	5:31:34	0.95	34°N130°E
11 June 2014	X1.0	9:01:33	9:06:02	9:22:55	0.34	44°N10°E

Nishimoto *et al. Earth, Planets and Space* (2023) 75:30

Page 10 of 15
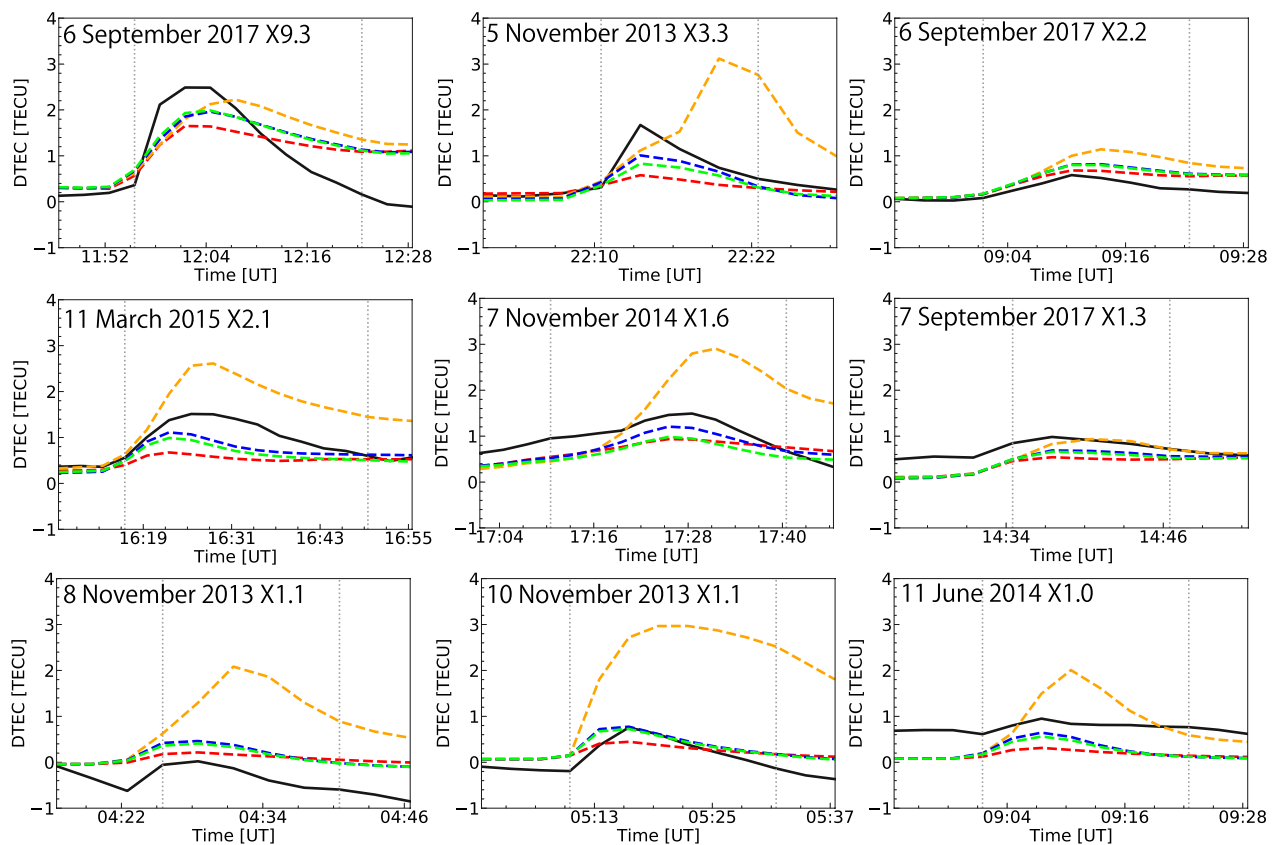
Fig. 7 Time variation of DTEC for the events analyzed in this study. The time variation of DTEC for the nine flare events analyzed in this study during the flare occurrence. The solid black, dashed red, dashed orange, dashed blue, and dashed green lines indicate the DTEC obtained from observations, RUN-Ff, RUN-FS35, RUN-FS15, and RUN-FS10, respectively. The observed and calculated DTEC were obtained at points, where the local time was around noon when each flare event occurred. The vertical dotted lines indicate, from left to right, the flare start and end times, respectively

wavelengths of solar flare emission that control the TEC enhancement. We verified the relationship between the observed and calculated DTEC, and between the observed and calculated solar flare emission spectra by statistically comparing nine flare events.

From Fig. 8, which shows the comparison between the observed and calculated values of SITEC, RUN-Ff tends to be smaller than the observed value; RUN-FS35 tends to be larger than the observed value, and both RUN-FS15 and RUN-FS10 reproduce the observed value of DTEC accurately. To consider the reason for this result, we focused on the solar flare emission spectra derived by FISM2 and the SFEM. The SFEM shows larger soft X-ray emission shorter than 10 nm than FISM2, and larger EUV emission at wavelengths of 10–11 nm, 28–29 nm, and 32–34 nm than FISM2 and SDO/EVE MEGS-A (Fig. 2). The dominant lines at wavelengths of 10–11 nm are high-temperature coronal lines, such as Fe XVII line and Fe XIX lines, while the dominant lines at 28–29 nm and 32–34 nm are relatively low-temperature coronal

lines, such as the Fe XV line and Fe XVI line, respectively. Thus, the difference in SITEC between RUN-Ff and RUN-FS10 is due to soft X-ray emission, the difference between RUN-FS15 and RUN-FS10 is due to high-temperature coronal line emissions, and the difference between RUN-FS35 and RUN-FS15 is due to relatively low-temperature coronal line emissions. Therefore, the SFEM could more accurately reproduce the total energy of soft X-ray emission and high-temperature coronal line emission. The high-temperature line emissions show the cooling process through the contribution function of various blend lines, which are known to be difficult to reproduce in empirical models (Chamberlin et al. 2020; Ryan et al. 2013). A physics-based model is a useful solution to this discrepancy. As shown in Figs. 5 and 6, the TEC enhancement by flare emission results in integrating the number of electrons in the D, E, and F regions, and the low-temperature coronal line emission that contributes to ionization in the F region is the most efficient contributor to the TEC enhancement. In fact, the
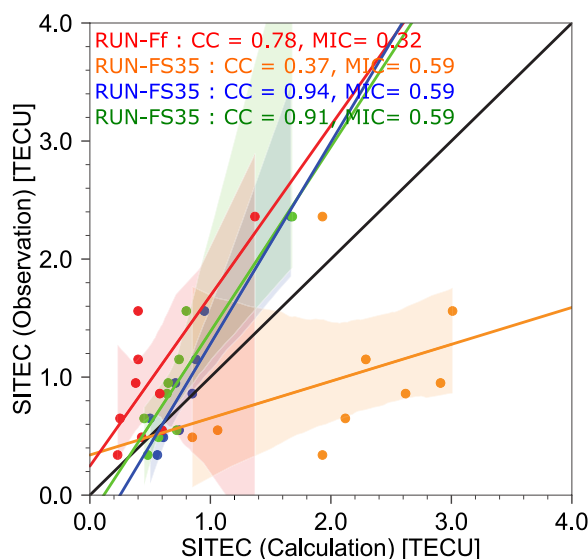
Fig. 8 Relationship between the observed and calculated SITEC for the events analyzed in this study. The relationship between the observed and calculated SITEC for the 9 flare events analyzed in this study. The results for RUN-Ff, RUN-FS35, RUN-FS15, and RUN-FS10 are plotted in red, orange, blue, and green, respectively. The dashed line shows the regression for each plot, and the black solid line shows a straight line with slope 1. For each regression line, 95% confidence intervals are shown in shading. The correlation coefficients (CC) and maximal information coefficient (MIC) are shown at the upper left, where the text color corresponds to the symbol color

photoionization and photo-dissociative ionization cross sections corresponding to the EUV emissions employed in GAIA are relatively large (see Fig. 5 of Watanabe et al. 2021). Furthermore, the timescale of electron recombination in the D and E regions of the ionosphere ionized by soft X-ray emission and high-temperature coronal line emission is a few minutes, whereas the timescale of recombination in the F region ionized by low-temperature coronal line emissions is, on average, hours, suggesting that low-temperature coronal line emissions are important for TEC enhancement (Zhang et al. 2011).
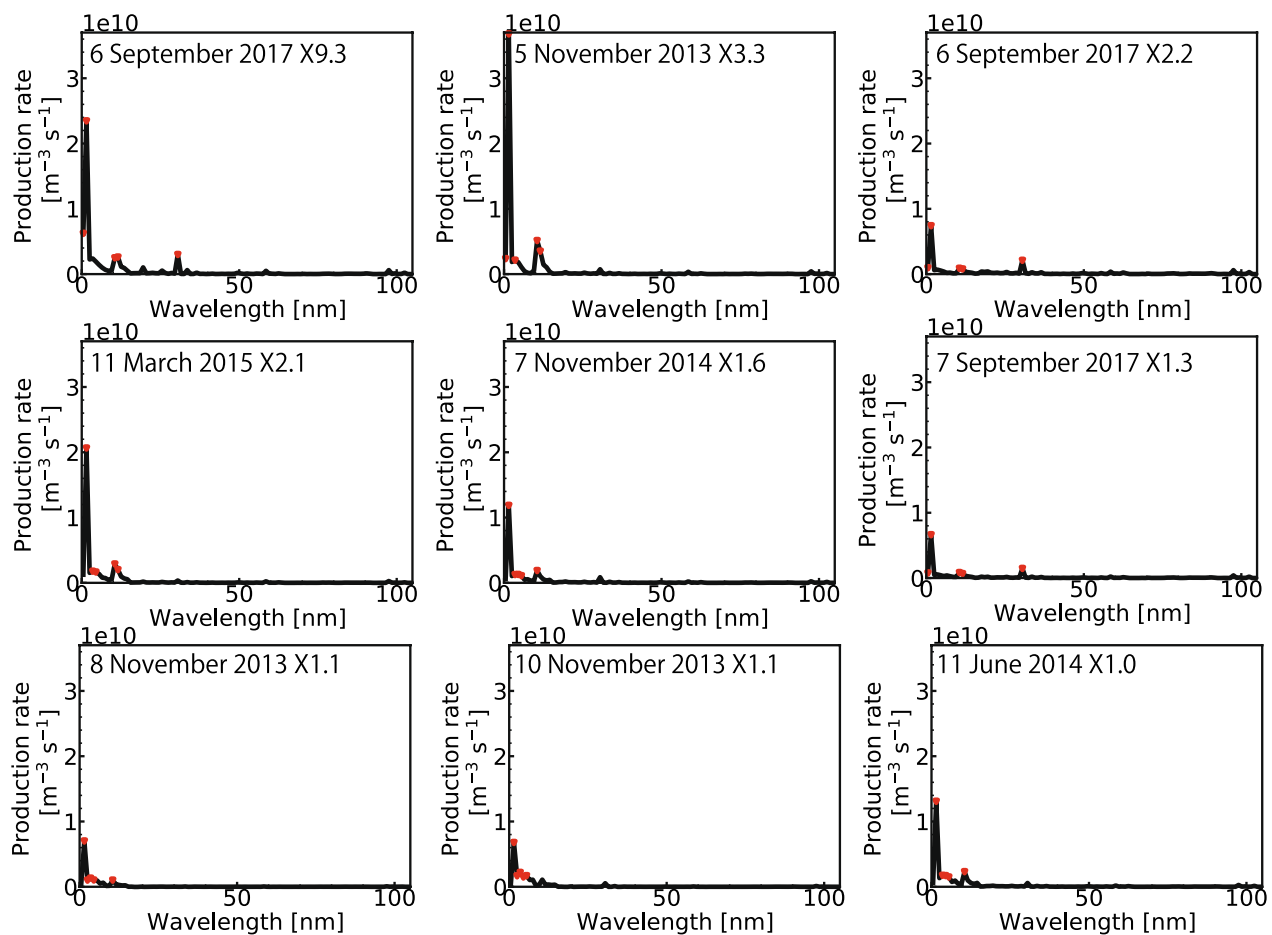
Figure 9 shows the solar emission and the difference in ion production rate between pre-flare and DTEC peak time. From Fig. 9, the neutral atmosphere is most ionized by soft X-ray emission, followed by EUV emission with a high formation temperature of 10–15 nm, and then EUV emission with a low formation temperature of 30–31 nm. Among these solar flare emissions, the wavelengths of soft X-ray and EUV emissions that contribute to the TEC enhancement are 1–2 nm and 10–11 nm and 30–31 nm, respectively. The dominant lines at these EUV emissions are Fe XVII 10.08 nm, Fe XIX 10.85 nm, and He II 30.38 nm. The He II line is strong solar emission in flare emission, which mainly ionizes the F layer and thus contributes efficiently to the TEC enhancement. The soft

X-ray emissions mainly ionize the D layer, which has a short time scale for recombination, and the photoionization and photo-dissociative ionization cross sections are also small. However, it is the most intense emission during flare, and its intensity is several orders of magnitude higher than that of EUV emission. In addition, photoelectron impact ionization becomes more than an order of magnitude greater than direct photoionization in this wavelength range (Solomon and Qian 2005). Therefore, its efficiency is poor, but it is expected to have an impact on the TEC variation. Furthermore, the soft X-ray and hot coronal line emissions were emitted from the optically thin solar corona and were not affected by the CLV. Therefore, the soft X-ray emission with a wavelength of 1–2 nm and Fe XVII and Fe XIX line emission are considered to be the best indicators of TEC enhancement.

In this study, the response of the ionosphere to solar flare emissions was investigated using the models for nine events with flare magnitude varying from X1.0–X9.3 and durations of 10–33 min. The observed SITEC variation for these flare events was 0.34–2.36 TECU. As shown in Fig. 8, solar cycle 24, mainly analyzed in this study, had low solar activity (Iijima et al. 2017; Imada et al. 2020) and did not produce any large-scale events that exceeded the X10 class. Furthermore, no flare events with EUV late phase, which is the second peak of the Fe XV and Fe XVI line emission, were found in this statistical study. It is possible that FISM2 and SFEM have not been able to reproduce the EUV late phase, but this cannot be confirmed due to the absence of SDO/EVE MEGS-A observations. Although the EUV late phase occurs in only about 13% of all flare events, it contributes to the ionization of the Earth's ionosphere, because its duration is longer than the flare main phase and its emission energy is larger (Woods et al. 2011). It is important to analyze large-scale flares and flares with EUV late phase from the perspective of space weather, because they have large emission energies and a large impact on the Earth's ionosphere. For future work, we need to continue to analyze flares with these characteristics that have occurred in the past and that will occur in solar cycle 25.

In this paper, we used only TEC as the ionospheric observation data. To evaluate the unusual electron density increase in the D and E regions related to the Dellinger effect in more detail, future work will require the use of ionosonde data (e.g., Tao et al 2020) and HF radar data (e.g., Watanabe and Nishitani 2013; Nishitani et al 2019; Chakraborty et al. 2021) and other ionospheric observation data.

The results of this study indicate that the TEC enhancement due to flare emission is determined by soft X-ray emission and EUV emission with wavelengths shorter than 35 nm. The TEC enhancement is found to be

Nishimoto *et al. Earth, Planets and Space* (2023) 75:30

Page 12 of 15

Fig. 9 Relationship between the solar emission and the difference in ion production rate. The relationship between the solar emission and the difference in ion production rate between pre-flare and DTEC peak time calculated by GAIA with RUN-FS15. The difference in ion production rate is the difference between the pre-flare and the DTEC peak time, integrated over height. Data from points where the local time was around noon at the time of each flare event are used. The red triangles in each panel indicate the top five wavelengths at which the ion production rate was the greatest

largely due to the change in the soft X-ray emission and EUV line emissions with wavelengths, such as Fe XVII 10.08 nm, Fe XIX 10.85 nm and He II 30.38 nm. Finally, we believe that the integration of the method introduced in this study, which uses the SFEM based on the physical processes of flare loops and the Earth's atmospheric model GAIA, into space weather forecasting will contribute to improving the forecast accuracy of space weather phenomena.

Abbreviations

AIA	Atmospheric Imaging Assembly
CANS	Coordinated Astronomical Numerical Software
CC	Correlation Coefficient
CLV	Center-to-Limb Variation
DTEC	Difference of Total Electron Content
EBTEL	Enthalpy-Based Thermal Evolution of Loops
EUV	Extreme Ultraviolet
EVE	Extreme ultraviolet Variability Experiment
FISM	Flare Irradiance Spectral Model
GCM	General Circulation Model
GAIA	Ground-to-Topside Model of Atmosphere and Ionosphere for Aeronomy
GOES	Geostationary Operational Environmental Satellite
ISEE	Institute for Space-Earth Environmental research
MAE	Mean Absolute Value
MEGS	Multiple EUV Grating Spectrograph
MIC	Maximal Information Coefficient
NICT	National Institute of Information and Communications Technology
SDO	Solar Dynamics Observatory
SIDs	Sudden Ionospheric Disturbances
SITEC	Sudden Increase in Total Electron Content
TEC	Total Electron Content
TECU	Total Electron Content Unit
UT	Universal Time
XRS	X-ray Sensor

Nishimoto *et al. Earth, Planets and Space*   (2023) 75:30

Page 13 of 15

Declarations

Author details
[1]National Defense Academy of Japan, 1-10-20 Hashirimizu, Yokosuka, Kanagawa 239-8686, Japan. [2]National Institute of Information and Communications Technology, 4-2-1, Nukui-Kitamachi, Koganei, Tokyo 184-8795, Japan. [3]Institute for Space-Earth Environmental Research (ISEE), Nagoya University, Furo-cho, Chikusa-ku, Nagoya, Aichi 464-8601, Japan. [4]Department of Earth and Planetary Science, University of Tokyo, 7-3-1, Hongo, Bunkyo-Ku, Tokyo 113-0033, Japan. [5]National Institute for Fusion Science, 322-6 Oroshi-cho, Toki, Gifu 509-5292, Japan.

References

Bornmann PL, Speich D, Hirman J, Matheson L, Grubb R, Garcia HA, Viereck R (1996) GOES X-ray sensor and its use in predicting solar-terrestrial disturbances. Proc SPIE 2812:291–298. https://doi.org/10.1117/12.254076

Cargill PJ, Bradshaw SJ, Klimchuk JA (2012) Enthalpy-based thermal evolution of loops. III. Comparison of zero-dimensional models. Astrophys J 758:5. https://doi.org/10.1088/0004-637x/758/1/5

Chakraborty S, Ruohoniemi JM, Baker JBH, Nishitani N (2018) Characterization of short-wave fadeout seen in daytime SuperDARN ground scatter observations. Radio Sci 53:472–484. https://doi.org/10.1002/2017RS006488

Chakraborty S, Baker JBH, Ruohoniemi JM, Kunduri B, Nishitani N, Shepherd SG (2019) A study of SuperDARN response to co-occurring space weather phenomena. Space Weather 17(9):1351–1363. https://doi.org/10.1029/2019sw002179

Chakraborty S, Qian L, Ruohoniemi JM, Baker JBH, Mclnerney JM, Nishitani N (2021) The role of flare-driven ionospheric electron density changes on the Doppler flash observed by SuperDARN HF radars. J Geophys Res Space Phys 126:e2021JA029300. https://doi.org/10.1029/2021JA029300

Chakraborty S, Qian L, Baker JBH, Ruohoniemi JM, Kuyeng K, Mclnerney JM (2022) Driving influences of the Doppler flash observed by SuperDARN HF radars in response to solar flares. J Geophys Res Space Phys 127:e2022JA030342. https://doi.org/10.1029/2022JA030342

Chamberlin PC, Woods TN, Eparvier FG (2007) Flare Irradiance Spectral Model (FISM): Daily component algorithms and results. Space Weather 5:S07005. https://doi.org/10.1029/2007SW000316

Chamberlin PC, Woods TN, Eparvier FG (2008) Flare Irradiance Spectral Model (FISM): Flare component algorithms and results. Space Weather 6:S05001. https://doi.org/10.1029/2007SW000372

Chamberlin PC, Eparvier FG, Knoer V, Leise H, Pankratz A, Snow M, Templeman B, Thiemann EMB, Woodraska DL, Woods TN (2020) The Flare Irradiance Spectral Model-Version 2 (FISM2). Space Weather 18:SW002588. https://doi.org/10.1029/2020SW002588

Curto JJ (2020) Geomagnetic solar flare effects: a review. J Space Weather Space Clim 10:27. https://doi.org/10.1051/swsc/2020027

Curto JJ, Marsal S, Blanch E, Altadill D (2018) Analysis of the solar flare effects of 6 September 2017 in the ionosphere and in the Earth's magnetic field using spherical elementary current systems. Space Weather 16:1709–1720. https://doi.org/10.1029/2018SW001927

Davies K (1990) Ionospheric radio. Peter Peregrinus Ltd., London. https://doi.org/10.1049/PBEW031E

Dellinger JH (1937) Sudden disturbances of the ionosphere. J Appl Phys 8:732–751. https://doi.org/10.1109/JRPROC.1937.228657

Dere KP, Landi E, Mason HE, Monsingnori BC, Young PR (1997) CHIANTI—an atomic database for emission lines. Astron Astrophys Suppl 125:149–173. https://doi.org/10.1051/0004-6361/201526827

Dere KP, Zanna GD, Young PR, Landi E, Sutherland RS (2019) CHIANTI—an atomic database for emission lines. XV. version 9, improvements for the X-ray satellite lines. Astrophys J Suppl 241:22. https://doi.org/10.3847/1538-4365/ab05cf

Donnelly RF (1969) Contribution of X-ray and EUV bursts of solar flares to sudden frequency deviations. J Geophys Res 74:1873–1877. https://doi.org/10.1029/JA074i007p01873

Fiori RAD, Koustov AV, Chakraborty S, Ruohoniemi JM, Danskin DW, Boteler DH, Shepherd SG (2018) Examining the potential of the super dual Auroral radar network for monitoring the space weather impact of solar X-Ray flares. Space Weather 16:1348–1362. https://doi.org/10.1029/2018SW001905

Fiori RAD, Chakraborty S, Nikitina L (2022) Data-based optimization of a simple shortwave fadeout absorption model. J Atmos Solar Terr Phys 230:105843. https://doi.org/10.1016/j.jastp.2022.105843

Fujiwara H, Miyoshi Y (2006) Characteristics of the large-scale traveling atmospheric disturbances during geomagnetically quiet and disturbed periods simulated by a whole atmosphere general circulation model. Geophys Res Lett 33:L20108. https://doi.org/10.1029/2006GL027103

Fujiwara H, Miyoshi Y (2009) Global structure of large-scale disturbances in the thermosphere produced by effects from the upper and lower regions: simulations by a whole atmosphere GCM. Earth Planets Space 61:463–470. https://doi.org/10.1186/BF03353163

Fujiwara H, Miyoshi Y (2010) Morphological features and variations of temperature in the upper thermosphere simulated by a whole atmosphere GCM. Ann Geophys 28:427–437. https://doi.org/10.5194/angeo-28-427-2010

Goncharenko LP, Tamburri CA, Tobiska WK, Schonfeld SJ, Chamberlin PC, Woods TN, Didkovsky L, Coster AJ, Zhang S-R (2021) A new model for ionospheric total electron content: the impact of solar flux proxies and indices. J Geophys Res 126:e2020JA028466. https://doi.org/10.1029/2020JA028466

Hofmann-Wellenhof B, Lichtenegger H, Collins J (1992) Global pointing system-theory and practice. Springer, New York. https://doi.org/10.1007/978-3-7091-5126-6

Iijima H, Hotta H, Imada S, Kusano K, Shiota D (2017) Improvement of solar-cycle prediction: plateau of solar axial dipole moment. Astron Astrophys 607:L2. https://doi.org/10.1051/0004-6361/201731813

Imada S, Matoba K, Fujiyama M, Iijima H (2020) Solar cycle-related variation in solar differential rotation and meridional flow in solar cycle 24. Earth Planets Space 72:182. https://doi.org/10.1186/s40623-020-01314-y

Jin H, Miyoshi Y, Fujiwara H, Shinagawa H (2008) Electrodynamics of the formation of ionospheric wave number 4 longitudinal structure. J Geophys Res 113:A09307. https://doi.org/10.1029/2008JA013301

Nishimoto *et al. Earth, Planets and Space*   (2023) 75:30

Page 14 of 15

Jin H, Miyoshi Y, Fujiwara H, Shinagawa H, Terada K, Terada N, Ishii M, Otsuka Y, Saito A (2011) Vertical connection from the tropospheric activities to the ionospheric longitudinal structure simulated by a new Earth's whole atmosphere-ionosphere coupled model. J Geophys Res 116:A01316. https://doi.org/10.1029/2010JA015925

Kawai T, Imada S, Nishimoto S, Watanabe K, Kawate T (2020) Nowcast of an EUV dynamic spectrum during solar flares. J Atmos Solar Terr Phys 205:105302. https://doi.org/10.1016/j.jastp.2020.105302

Klimchuk JA, Patsourakos S, Cargill PJ (2008) Highly efficient modeling of dynamic coronal loops. Astrophys J 682:1351–1362. https://doi.org/10.1086/589426

Kusano K, Ichimoto K, Ishii M, Miyoshi Y, Yoden S, Akiyoshi H, Asai A, Ebihara Y, Fujiwara H, Goto T-N, Hanaoka Y, Hayakawa H, Hosokawa K, Hotta H, Hozumi K, Imada S, Iwai K, Iyemoti T, Jin H, Kataoka R, Katoh Y, Kikuchi T, Kubo Y, Kurita S, Matsumoto H, Mitani T, Miyahara H, Miyoshi Y, Nagatsuma T, Nakamizo A, Nakamura S, Nakata H, Nishizuka N, Otsuka Y, Saito S, Saito S, Sakurai T, Sato T, Shimizu T, Shinagawa H, Shiokawa K, Shiota D, Takashima T, Tao C, Toriumi S, Ueno S, Watanabe K, Watari S, Yashiro S, Yoshida K, Yoshikawa A (2021) PSTEP: project for solar-terrestrial environment prediction. Earth Planets Space 73:159. https://doi.org/10.1186/s40623-021-01486-1

Lemen JR, Title AM, Akin DJ, Boerner PF, Chou C, Drake JF, Duncan DW, Edwards CG, Friedlaender FM, Heyman GF, Hurlburt NE, Katz NL, Kushner GD, Levay M, Lindgren RW, Mathur DP, McFeaters EL, Roger SM, Rehse A, Chrijver CJ, Springer LA, Stern RA, Tarbell TD, Wuelser J-P, Wolfson CJ, Yanari C, Bookbinder JA, Cheimets PN, Caldwell D, Deluca EE, Gates R, Golub L, Park S, Podgorski WA, Bush RI, Scherrer PH, Gummin MA, Smith P, Auker G, Jerram P, Pool P, Soufli R, Windt DL, Beardsley S, Clapp M, Lang J, Waltham N (2012) The atmospheric imaging assembly (AIA) on the solar dynamics observatory (SDO). Solar Phys 275:17–40. https://doi.org/10.1007/s11207-011-9776-8

Mitra AP (1974) Ionospheric effects of solar flares. Springer, Dordrecht. https://doi.org/10.1007/978-94-010-2231-6

Miyoshi Y, Fujiwara H (2003) Day-to-day variations of migrating diurnal tide simulated by a GCM from the ground surface to the exobase. Geophys Res Lett 30(15):1789. https://doi.org/10.1029/2003GL017695

Miyoshi Y, Fujiwara H (2006) Excitation mechanism of intraseasonal oscillation in the equatorial mesosphere and lower thermosphere. J Geophys Res 111:D14108. https://doi.org/10.1029/2005JD006993

Miyoshi Y, Fujiwara H (2008) Gravity waves in the thermosphere simulated by a general circulation model. J Geophys Res 113:D01101. https://doi.org/10.1029/2007JD008874

Nishimoto S, Watanabe K, Kawai T, Imada S, Kawate T (2021) Validation of computed extreme ultraviolet emission spectra during solar flares. Earth Planets Space 73:79. https://doi.org/10.1186/s40623-021-01402-7

Nishitani N, Ruohoniemi JM, Lester M, Baker JBH, Koustov AV, Shepherd SG, Chisham G, Hori T, Thomas EG, Makarevich RA, Marchaudon A, Poromarenko P, Wild JA, Milan SE, Bristow WA, Devlin J, Miller E, Greenwald RA, Ogawa T, Kikuchi T (2019) Review of the accomplishments of midlatitude Super Dual Auroral Radar Network (SuperDARN) HF radars. Prog Earth Planet Sci 6:27. https://doi.org/10.1186/s40645-019-0270-5

Otsuka Y, Ogawa T, Saito A, Tsugawa T, Fukao S, Miyazaki S (2002) A new technique for mapping of total electron content using GPS network in Japan. Earth Planets Space 54(1):63–70. https://doi.org/10.1186/BF03352422

Qian L, Burns AG, Chamberlin PC, Solomon SC (2010) Flare location on the solar disk: modeling the thermosphere and ionosphere response. J Geophys Res 115:A09311. https://doi.org/10.1029/2009JA015225

Qian L, Burns AG, Chamberlin PC, Solomon SC (2011) Variability of thermosphere and ionosphere responses to solar flares. J Geophys Res 116:A10309. https://doi.org/10.1029/2011JA016777

Qian L, Wang W, Burns AG, Chamberlin PC, Coster A, Zhang S-R, Solomon SC (2019) Solar flare and geomagnetic storm effects on the thermosphere and ionosphere during 6–11 September 2017. J Geophys Res 124:2298–2311. https://doi.org/10.1029/2018JA026175

Reshef DN, Reshef YA, Finucane HK, Grossman SR, Mcvean G, Turnbaugh PJ, Lander ES, MitzenmacherSabeti MPC (2011) Detecting novel associations in large data sets. Science 334(6062):1518–1524. https://doi.org/10.1126/science.1205438

Richards PG, Fennelly JA, Torr DG (1994) EUVAC: a solar EUV flux model for aeronomic calculations. J Geophys Res 99(A5):8981. https://doi.org/10.1029/94JA00518

Ryan DF, Chamberlin PC, Milligan RO, Gallagher PT (2013) Decay-phase cooling and inferred heating of Mand X-class solar flares. Astrophys J 778(1):68. https://doi.org/10.1088/0004-637X/778/1/68

Scherliess L, Tsagouri I, Yizengaw E, Bruinsma S, Shim JS, Coster A, Retterer JM (2019) The international community coordinated modeling center space weather modeling capabilities assessment: overview of ionosphere/thermosphere activities. Space Weather 17:527–538. https://doi.org/10.1029/2018SW002036

Shinagawa H, Oyama S (2006) A two-dimensional simulation of thermospheric vertical winds in the vicinity of an auroral arc. Earth Planets Space 58:1173–1181. https://doi.org/10.1186/BF03352007

Shinagawa H, Iyemori T, Saito T, Maruyama T (2007) A numerical simulation of ionospheric and atmospheric variations associated with the Sumatra earthquake on December 26, 2004. Earth Planets Space 59:1015–1026. https://doi.org/10.1186/BF03352042

Shinbori A, Otsuka Y, Sori T, Tsugawa T, Nishioka M (2020) Temporal and spatial variations of total electron content enhancements during a geomagnetic storm on 27 and 28 September 2017. J Geophys Res. https://doi.org/10.1029/2019JA026873

Solomon SC, Qian L (2005) Solar extreme-ultraviolet irradiance for general circulation models. J Geophys Res 110:A10306. https://doi.org/10.1029/2005JA011160

Tao C, Nishioka M, Saito S, Shiota D, Watanabe K, Nishizuka N, Tsugawa T, Ishii M (2020) Statistical analysis of short-wave fadeout for extreme space weather event estimation. Earth Planets Space 72(1):173. https://doi.org/10.1186/s40623-020-01278-z

Thiemann EMB, Eparvier FG, Woods TN (2017) A time dependent relation between EUV solar flare light-curves from lines with differing formation temperatures. J Space Weather Space Clim 7:A36. https://doi.org/10.1051/swsc/2017037

Tsugawa T, Sadakane T, Sato J, Otsuka Y, Ogawa T, Shiokawa K, Saito A (2006) Summer-winter hemispheric asymmetry of sudden increase in ionospheric total electron content induced by solar flares: A role of O/N_2 ratio. J Geophys Res 111:A11316. https://doi.org/10.1029/2006JA011951

Tsugawa T, Nishioka M, Ishii M, Hozumi K, Saito S, Shinbori A, Otsuka Y, Saito A, Buhari SM, Abdullah M, Supnithi P (2018) Total electron content observations by dense regional and worldwide international networks of GNSS. J Disaster Res 13(3):535–545. https://doi.org/10.20965/jdr.2018.p0535

Tsurutani BT, Verkhoglyadova OP, Mannucci AJ, Lakhina GS, Zank GP (2009) A brief review of "solar flare effects" on the ionosphere. Radio Sci 44:1–14. https://doi.org/10.1029/2008RS004029

Watanabe D, Nishitani N (2013) Study of ionospheric disturbances during solar flare events using the SuperDARN Hokkaido radar. Adv Polar Sci 24(1):12–18. https://doi.org/10.3724/SPJ.1085.2013.00012

Watanabe K, Masuda S, Segawa T (2012) Hinode flare catalogue. Sol Phys 279:317–322. https://doi.org/10.1007/s11207-012-9983-y

Watanabe K, Jin H, Nishimoto S, Imada S, Kawai T, Kawate T, Otsuka Y, Shinbori A, Tsugawa T, Nishioka M (2021) Model-based reproduction and validation of the total spectrum of solar flare and their impact on the global environment at the X9.3 event of September 6 2017. Earth Planets Space 73:96. https://doi.org/10.1186/s40623-021-01376-6

Woods TN, Kopp G, Chamberlin PC (2006) Contributions of the solar ultraviolet to the total solar irradiance during large flares. J Geophys Res 111:10S14. https://doi.org/10.1029/2005JA011507

Woods TN, Hock R, Eparvier F, Jones AR, Chamberlin PC, Klimchuk JA, Didkovsky L, Judge D, Mariska J, Warren H, Schrijver CJ, Webb DF, Bailey S, Tobiska WK (2011) New solar extreme-ultraviolet irradiance observations during flares. Astrophys J 739:59. https://doi.org/10.1088/0004-637X/739/2/59

Woods TN, Eparvier FG, Hock R, Jones AR, Woodraska D, Judge D, Didkovsky L, Lean J, Mariska J, Warren H, McMullin D, Chamberlin P, Berthiaume G, Bailey S, Fuller-Rowell T, Sojka J, Tobiska WK, Viereck R (2012) Extreme ultraviolet variability experiment (EVE) on the solar dynamics observatory (SDO): overview of science objectives, instrument design, data products, and model developments. Solar Phys 275:115–143. https://doi.org/10.1007/s11207-009-9487-6

Worden JR, Woods TN, Bowman KW (2001) Far-ultraviolet intensities and center-to-limb variations of active regions and quiet Sun using UARS SOLSTICE irradiance measurements and ground-based spectroheliograms. Astrophys J 560:1020. https://doi.org/10.1086/323058

Nishimoto *et al. Earth, Planets and Space*   (2023) 75:30

Page 15 of 15

Yasyukevich Y, Astafyeva E, Padokhin A, Ivanova V, Syrovatskii S, Podlesnyi A (2018) The 6 September 2017 X-class solar flares and their impacts on the ionosphere, GNSS, and HF radio wave propagation. Space Weather 16:1013–1027. https://doi.org/10.1029/2018SW001932

Zhang DH, Mo XH, Cai L, Zhang W, Feng M, Hao YQ, Xiao Z (2011) Impact factor for the ionospheric total electron content response to solar flare irradiation. J Geophys Res 116:A04311. https://doi.org/10.1029/2010JA016089

Snow M, Mcclintock WE, Woods TN, White OR, Harder JW, Rottman G (2005) The Mg II Index from SORCE. SolPhys 230:325–344.

Publisher's Note

Springer Nature remains neutral with regard to jurisdictional claims in published maps and institutional affiliations.